



CHALMERS
UNIVERSITY OF TECHNOLOGY

Particle–droplet coalescence and jumping on superhydrophobic surfaces – A direct numerical simulations study

Downloaded from: <https://research.chalmers.se>, 2025-06-01 14:59 UTC

Citation for the original published paper (version of record):

Konstantinidis, K., Göhl, J., Mark, A. et al (2024). Particle–droplet coalescence and jumping on superhydrophobic surfaces – A direct numerical simulations study. *Physics of Fluids*, 36(8). <http://dx.doi.org/10.1063/5.0222367>

N.B. When citing this work, cite the original published paper.

RESEARCH ARTICLE | AUGUST 27 2024

Particle–droplet coalescence and jumping on superhydrophobic surfaces—A direct numerical simulations study ^{EP}

K. Konstantinidis ; J. Göhl ; A. Mark ; X. Yan ; N. Miljkovic ; S. Sasic 



Physics of Fluids 36, 082117 (2024)

<https://doi.org/10.1063/5.0222367>



Articles You May Be Interested In

Coalescence-induced jumping of droplets from superhydrophobic surfaces—The effect of contact-angle hysteresis

Physics of Fluids (November 2022)

Effects of protuberant structure on coalescence-induced jumping of droplets on superhydrophobic surfaces

Physics of Fluids (August 2023)

Enhancement of coalescence-induced nanodroplet jumping on superhydrophobic surfaces with designed structures

Physics of Fluids (April 2025)



Physics of Fluids

Special Topics Open
for Submissions

[Learn More](#)

Particle–droplet coalescence and jumping on superhydrophobic surfaces—A direct numerical simulations study

Cite as: Phys. Fluids **36**, 082117 (2024); doi:10.1063/5.0222367

Submitted: 7 June 2024 · Accepted: 7 August 2024 ·

Published Online: 27 August 2024



View Online



Export Citation



CrossMark

K. Konstantinidis,^{1,a)}  J. Göhl,²  A. Mark,^{1,2}  X. Yan,^{3,4,5}  N. Miljkovic,^{5,6,7,8,9}  and S. Sasic¹ 

AFFILIATIONS

¹Division of Fluid Dynamics, Department of Mechanics and Maritime Sciences, Chalmers University of Technology, Gothenburg SE-412 96, Sweden

²Fraunhofer-Chalmers Center, Chalmers Science Park, Gothenburg SE-412 88, Sweden

³Key Laboratory of Low-Grade Energy Utilization Technologies and Systems, Chongqing University, Ministry of Education, Chongqing 400030, China

⁴Institute of Engineering Thermophysics, Chongqing University, Chongqing 400030, China

⁵Department of Mechanical Science and Engineering, University of Illinois, Urbana, Illinois 61801, USA

⁶Department of Electrical and Computer Engineering, University of Illinois, Urbana, Illinois 61801, USA

⁷Materials Research Laboratory, University of Illinois, Urbana, Illinois 61801, USA

⁸Institute for Sustainability, Energy and Environment (iSEE), University of Illinois, Urbana, Illinois 61801, USA

⁹International Institute for Carbon Neutral Energy Research (WPI-I2CNER), Kyushu University, 744 Moto-oka Nishi-ku, Fukuoka 819-0395, Japan

^{a)}Author to whom correspondence should be addressed: konkonst@chalmers.se

ABSTRACT

We report here multiphase direct numerical simulations of a recently discovered passive mechanism of self-cleaning on superhydrophobic surfaces. The removal of contaminants is governed by coalescence of a single droplet with a particle of micrometer size, where the droplet initiates spontaneous spreading on the particle and drives particle–droplet jumping. We use an in-house volume of fluid–immersed boundary numerical framework, introduce and thoroughly analyze capillary forces at the particle–droplet contact line, and validate our simulations in relation to previous experimental results. We then perform a comprehensive investigation over a number of different parameters regarding the interaction physics of the droplet with the particle and the substrate. We systematically vary particle, droplet, and surface physical and wetting properties and unveil a range of scenarios related to different energy dissipation mechanisms as a function of the substrate contact angles and contact-angle hysteresis. Detailed parameter studies establish the connection between the droplet, substrate and particle properties, and the outcome and efficiency of the particle-launching process. We particularly highlight the effects of the particle–droplet size ratio and the wettability of the particle. We reveal and discuss the corresponding dissipation mechanisms and quantify the energy efficiencies of the jumping process in the treated parameter space.

© 2024 Author(s). All article content, except where otherwise noted, is licensed under a Creative Commons Attribution (CC BY) license (<https://creativecommons.org/licenses/by/4.0/>). <https://doi.org/10.1063/5.0222367>

I. INTRODUCTION

In the field of surface technology, preserving the surface properties becomes a challenge due to contamination caused by solid particles and microbiological agents. These contaminants deteriorate the functionality of the surfaces that are used in numerous applications, such as defrosting, deicing, and heat-exchanging condensers.^{1–3} To address

this problem, surface modifications have been suggested, particularly focused on achieving hydrophobicity.^{4,5} The design of such surfaces was initially inspired by the water-repellent behavior that certain organisms have developed in nature. These organisms demonstrate natural self-cleaning on their surfaces, with some examples being lotus plant leaves and cicada wings.⁶ They have developed micro- and

nano-scale structures to repel water and remove contaminants by droplet motion.^{7–10} Studies have shown that by reproducing patterns with micro- and nano-scale structures, contact angles of 170° and above were achieved, while the sliding angle and hysteresis remained below 2° .^{11,12}

A significant challenge related to a successful industrial application of these bio-mimicking superhydrophobic surfaces is how to improve their durability. Typical estimated lifetimes of these low-adhesion surfaces are often short,^{3,13,14} but recent studies suggest that the life-cycle of superhydrophobic surfaces can be significantly extended.^{9,12} This makes the need for understanding mechanisms and devising techniques for cleaning (including self-cleaning) of such surfaces even more industrially relevant.

Multiple ways to remove particles from surfaces have been suggested in the literature, with studies explaining the dynamics of removal when an initial velocity for a liquid phase is present¹⁵ or an air flow stream carries the particles away harnessing inertia.¹⁶ Gravity often contributes as an external supporting mechanism, leading droplets to roll off the substrate, while they capture and remove particles from the surface in the process.^{4,17} In addition to the mentioned active cleaning mechanisms, there is a need for devising passive mechanisms that use droplets to remove the contaminants and require no presence of an external field.

A recently suggested and very popular passive mechanism for the removal of contaminants is a somewhat counter-intuitive phenomenon of droplet coalescence and jumping on superhydrophobic surfaces.^{18,19} Wisdom *et al.*²⁰ were one of the first to explore the self-cleaning benefits of the phenomenon, but effort was foremost focused on the physics behind the eventual jumping.^{19,21–23} The interest associated with this mechanism was mainly attributed to the absence of external contribution instigating the jumping,²¹ and the phenomenon was studied extensively, both experimentally and numerically, to uncover the factors that affect its efficiency,^{24,25} influence of the initial velocity,^{26,27} or the existence of grooves,²⁸ which all can significantly increase the jumping velocity. The surface energy released during coalescence is translated into the kinetic energy that propels the merged droplet. The total energy gained by the droplets can vary, and it is influenced by surface modifications that promote a Cassie–Baxter wetting stage.^{29–31} In our previous study,³² we emphasized the strong connection between the values for advancing and receding contact angles and the energy losses. We also studied and quantified how hysteresis and the appearance of a dynamic contact angle variation increase dissipation. We have shown that the accurate capturing of the merged droplet contact line movement and the droplets' oscillations leads to a more accurate prediction of the energy losses at the contact line. We note that most of these studies have only focused on the coalescence and jumping of droplets, without considering the presence and influence of contaminants on the jumping process. The only work that we are aware of that studied numerically the removal of a spherical particle by binary droplet coalescence and jumping³³ used the lattice-Boltzmann method to model the fluids and a separate model for the capillary forces.³⁴ In that study, the particle was already encapsulated in the droplet, a condition that is not very physically relevant.

In a recent work, Yan *et al.*³⁵ reported a different passive mechanism for self-cleaning, based on coalescence (and subsequent jumping) of a single droplet and a particle. The authors studied the phenomenon experimentally and performed momentum and wetting analyses to

identify the effects of particle/droplet properties and wettabilities. The process starts with the liquid bridge forming during the initial droplet spreading on the particle (referred to as the spreading liquid front) and interacting with the superhydrophobic surface and eventually pushing the particle–droplet system upward with a specific jumping velocity. The key factor behind this mechanism is the wettability of the particle (especially for hydrophilic particles), which reduces the overall surface energy of the system during the droplet spreading phase. A part of this energy is converted into the kinetic energy of the particle–droplet system. In some cases, the aggregate attains a jumping velocity similar to that of jumping droplets. Moreover, the particle–droplet system shows rotation due to the size and weight mismatch of the particle and the droplet, while an oblique upward direction may appear when the merged system is lifted from the solid surface.

This mentioned work³⁵ indeed provided significant information related to this novel passive self-cleaning mechanism, but certain details can be uncovered solely by numerical simulations that fully resolve the contact-line physics and capillary wave dynamics taking place during droplet–particle coalescence and jumping. A fundamental challenge, but also one of the major contributions of such numerical studies, is to establish the connection between adhesion of the particle to the droplet and inertia of the liquid bridge at the early spreading stage. In the mentioned numerical study,³³ the system was initiated with the particle partially wetted in equilibrium or fully encapsulated in a droplet. This leads us to conclude that there is great relevance in investigating the wetting of a particle surface from a fully dry state, and in that way identifying the driving factors for spreading dynamics, estimating the energy losses during spreading of the droplet on the particle, and studying the interaction of the oscillating droplet with the substrate. The present study provides qualitative and quantitative information about these characteristics and their influence on the jumping process by fully resolving the relevant physics and investigating different particle, droplet, or wetting properties. By creating a relevant parameter space (mirrored by the cases we will run), we will identify and quantify the influence of these parameters to the overall efficiency of the proposed mechanism.

The novelty and complexity of the task are highlighted by the absence of similar numerical studies. Numerous challenges exist in studying numerically the dynamics of complex interfaces, movement of a three-phase contact line, and wetting of a (highly) curved boundary such as that of the particle surface. The most important ones comprise the lack of knowledge related to the adhesion physics, particularly in the dynamic spreading during the liquid bridge formation and the limited (and insufficiently validated) models formulated to describe capillarity adhesion in Eulerian frameworks. The capillary forces on the particle from the droplet result from a line tension force acting at the three-phase contact line. The total of these forces combines the effects of the van der Waals bonds, electrostatic forces, and capillarity. The direction and magnitude of the resulting force are described and modeled for static applications such as colloids in rest,^{36,37} captured contaminants,³⁸ or elastic solids.³⁹ However, we expect that the contact-line dynamics has a strong effect on the adhesive capillary force acting on the particle. So, any numerical framework that aspires to study this self-cleaning mechanism needs to successfully deal with three fundamental factors: (i) the contact line movement on the superhydrophobic surface, (ii) the spreading of the droplet on the curved particle surface, and (iii) the very small temporal and spatial

scales determined by the fluid properties and droplet and/or particle sizes. In addition, it is not to be forgotten that the movement of the particle in space, as a result of the acting forces, creates an additional complexity since the numerical framework needs to account for the volume of the solid, which will be populated by the fluid and vice versa. To achieve these goals, we combine in this work an immersed boundary method (IBM)⁴⁰ with a sharp interface representation in an Eulerian framework.

Hence, this study addresses the aforementioned challenges and introduces a comprehensive and robust numerical method able to describe all stages of the particle–droplet coalescence and jumping process. The method comprises a combined volume of fluid (VOF)–IBM approach that is for the first time, to the best of the authors’ knowledge, used for this type of problems. We also note that other studies used VOF–IBM solvers previously, for example, for a water flooding process,⁴¹ droplets and wetting cylinders,^{42,43} droplet–particle interactions,⁴⁴ and wetting of non-spherical particles.⁴⁵ Specifically, we are particularly interested in accurately capturing the initial spreading phase for which only limited information can be extracted through experimental studies. We will improve the understanding of that phase of the process by looking in great detail at the liquid spreading on a curved surface, the partial contact of the droplet with the substrate, and the eventual launch of the particle–droplet system into the air. Furthermore, a comprehensive study will be conducted regarding the variations in the kinetic and surface energies of the system, along with an analysis of the total energy budgets for systematically varied droplet, particle, and surface properties. Our results will highlight, among other things, the key mechanisms of total viscous dissipation before and after particle–droplet departure.

The paper is organized as follows: in Sec. II, we describe in detail our numerical framework and how we configure our simulations and calculate fundamental geometrical and dynamical properties of the system (Sec. III). A thorough validation process is presented in Sec. IV. In Sec. V, we present and discuss our results and go through individual effects of the chosen geometrical and wetting properties of the system. Finally, in Sec. VI, we summarize our findings and implications of our study and present suggestions for possible directions of future work.

II. METHODS

We carried out the simulations using an in-house Multiphysics flow solver called IPS IBOFlow[®]. To handle two-phase flow and moving objects, the solver combines the volume-of-fluid (VOF) method with the mirroring immersed boundary method.⁴⁶ The two-phase flow is governed by a single-fluid equation, solved for the velocity \mathbf{v} and pressure p ,

$$\nabla \cdot \mathbf{v} = 0, \tag{1}$$

$$\frac{\partial(\rho\mathbf{v})}{\partial t} + \mathbf{v} \cdot \nabla(\rho\mathbf{v}) = -\nabla p + \nabla \cdot (\mu\nabla\mathbf{v}) + \rho\mathbf{g} + \mathbf{f}_{SF}.$$

The density ρ and dynamic viscosity μ depend on the interface location, \mathbf{g} stands for the gravitational acceleration, and \mathbf{f}_{SF} is the normal surface tension force per unit volume acting at the interface. The coupling of pressure and velocity is performed with the segregated SIMPLEC method,⁴⁷ while discretization is performed on an adaptive octree, co-located grid.

The movement of the interface between the liquid and gas phases is captured using the VOF method. It is a sharp-interface method, which solves a transport equation for the volume fraction field,

$$\frac{\partial\alpha}{\partial t} + \mathbf{v} \cdot \nabla\alpha = 0, \tag{2}$$

where α is the volume fraction. The transport equation is discretized using the CICSAM⁴⁸ convective scheme, which is a higher-order scheme that is fully conservative and bounded, achieving an improved sharp-interface movement.

Next, the fluid properties are obtained by volume averaging using the updated interface location,

$$\rho = \alpha\rho_1 + (1 - \alpha)\rho_2, \tag{3}$$

$$\mu = \alpha\mu_1 + (1 - \alpha)\mu_2, \tag{4}$$

where the sub-indices represent the two different phases. The surface tension body force \mathbf{f}_{SF} is given by the continuum surface force (CSF)⁴⁹ model,

$$\mathbf{f}_{SF} = \sigma\kappa\mathbf{n}, \tag{5}$$

where σ is the surface tension between liquid and gas, κ is the interface curvature, and \mathbf{n} is the interface normal vector. In this method, the latter is provided by the gradient of the volume fraction $\nabla\alpha$, which reaches asymptotically maximum at the actual location of the interface.

To obtain the curvature κ of the interface, we compute the divergence of the unit vector normal to the interface $\hat{\mathbf{n}}$. For its estimation, an improvement in the volume fraction gradient is attained with artificially diffusing the interface by performing a series of Laplacian filterings⁵⁰ in the volume fraction field, which is a technique that ensures accuracy even for highly distorted interfaces. Tests suggested that a repetition of ten times of the filtering process was required for treating wetting phenomena with the presence of strong capillary forces.⁵¹ The equations for $\hat{\mathbf{n}}$ and κ read

$$\hat{\mathbf{n}} = \frac{\tilde{\mathbf{n}}}{\|\tilde{\mathbf{n}}\|} = \frac{\nabla\tilde{\alpha}}{\|\nabla\tilde{\alpha}\|}, \tag{6}$$

$$\kappa = -\nabla \cdot \hat{\mathbf{n}}. \tag{7}$$

To counter issues stemming from the nature of co-located grids, we use the balanced-force method^{52,53} in the momentum equation [Eq. (1)]. This method provides improved values for the velocities at the faces by accounting contributions from the forces and the pressure gradient. Crucially, it also includes the surface tension body force for the cells near the interface and helps to balance the variations in the velocity field due to the phase change. Moreover, it contains a time derivative in the velocity interpolation. This stable method for the face velocities reduces spurious currents and avoids oscillations caused by pressure instabilities. The correct implementation of this method has been considered key in achieving perfect advection of the sharp interface on top of curved surfaces. Our framework is able to capture the interface even for the smallest length scales that appeared in our study.

To account for the wetting of a particle, the contact angle is imposed at the particle surface in the same manner as we did for droplets in our previous works.^{51,54} In summary, a Neumann boundary condition is implemented for the volume fraction in the vicinity of the immersed boundary. A correction for ghost cells near the contact line

is used where the volume fraction is extrapolated to the ghost cell from the main field, in the tangential direction of the interface. We consider important to separate advancing and receding behaviors. We have tested here using both a constant contact angle for each wetting motion, and to let the framework compute the angles from a dynamic contact angle model, dependent on the contact line velocity.^{55–57} A contact angle is always imposed with reference to the normal vector at the surface of the solid body. Additionally, the Navier-slip boundary condition is used for the superhydrophobic substrate, to account for roughness effects and to deal with the stress singularity problem.⁵⁴

The mirroring IBM sets the presence of solid objects in an Eulerian field by calculating the location of its triangulated boundary surfaces and implementing implicitly the corresponding boundary conditions in the cells that are populated by solid near the solid surface. The normal vector of the boundary surfaces $\hat{\mathbf{n}}_{ds}$ is used to set the corresponding normal and tangential velocities, as well as the pressure boundaries, which are obtained with interpolation of the pressure from the fluid cells to the boundary location. In addition, the fluid shear rate is obtained at the center of the triangle of the boundary, tangential to the boundary, using the values at the mirrored ghost cells. This approach does not require further changes to the gradient computation, as the gradients dictate the velocities at the center of the mirrored cells.^{40,46} The total hydrodynamic force acting on the particle is computed by

$$\mathbf{F}_{IB} = \int_{A_{tr}} \mathbf{t}_{ds} \cdot \hat{\mathbf{n}}_{ds} dS, \quad (8)$$

where the fluid stress tensor is given by

$$\mathbf{t}_{ds} = -p\mathbf{I} + \mu(\nabla\mathbf{v} + (\nabla\mathbf{v})^T). \quad (9)$$

The total torque is calculated by

$$\mathbf{T}_{IB} = \int_{A_{tr}} \mathbf{r} \times (\mathbf{t}_{ds} \cdot \hat{\mathbf{n}}_{ds}) dS. \quad (10)$$

In the case of partial wetting, the adhesive force exerted on the particle by the droplet arises from the line force acting at the triple-phase contact line.^{38,58} The exact equation for the adhesive capillary force \mathbf{F}_{cap} at contact line C_l , when the interface is at rest, is obtained by

$$\mathbf{F}_{cap} = \int_{C_l} \sigma \hat{\mathbf{t}}_{int} dl, \quad (11)$$

where $\hat{\mathbf{t}}_{int}$ is the unit vector tangential to the interface, originating from the contact line. Here, $\hat{\mathbf{t}}_{int}$ can be computed from the normal $\hat{\mathbf{n}}$ of the interface at the contact line and the normal vector of the object surface $\hat{\mathbf{n}}_{ds}$ with vector analysis,

$$\hat{\mathbf{t}}_{int} = \frac{\hat{\mathbf{n}}_{ds} - (\hat{\mathbf{n}} \cdot \hat{\mathbf{n}}_{ds})\hat{\mathbf{n}}}{\|\hat{\mathbf{n}}_{ds} - (\hat{\mathbf{n}} \cdot \hat{\mathbf{n}}_{ds})\hat{\mathbf{n}}\|}. \quad (12)$$

Washino *et al.*⁵⁹ introduced the continuum capillary force method (CCF) to directly estimate the force exerted on a solid surface due to the presence of an interface of the fluid that spreads on that surface. It follows an approach similar to the CSF model in VOF,⁴⁹ which involves integrating the volume fraction gradient across a cell to locate the interface location and direction. With this technique to account for the existence of two interfaces, the method is able to estimate the

location of the contact line from their intersection. In CCF, a field χ denoting the solid volume fraction is generated, imposing a smooth transition between phases, in order to compute the Eulerian gradient of the solid volume fraction. The contact line is then obtained from the volume integral of two Dirac functions,^{59,60} corresponding to the liquid–gas interface location with tangential direction to the solid and the solid–fluid boundary normal. Both are integrated over the volume of a cell to compute the line force in that cell.

The developed model, which estimates a body force for a cell that contains the contact line, reads

$$\mathbf{f}_{CCF} = \sigma \mathbf{t}_{int} (\nabla\alpha \cdot \mathbf{t}_{C_l}) (\nabla\chi \cdot \mathbf{n}_{ds}). \quad (13)$$

The tangential unit vector to the wall pointing away from the interface is computed from the unit normals as follows:

$$\hat{\mathbf{t}}_{C_l} = \frac{\hat{\mathbf{n}} - (\hat{\mathbf{n}}_{ds} \cdot \hat{\mathbf{n}})\hat{\mathbf{n}}_{ds}}{\|\hat{\mathbf{n}} - (\hat{\mathbf{n}}_{ds} \cdot \hat{\mathbf{n}})\hat{\mathbf{n}}_{ds}\|}. \quad (14)$$

The total capillary force \mathbf{F}_{CCF} and torque \mathbf{T}_{CCF} can then be computed in the fluid (Eulerian) domain as

$$\mathbf{F}_{CCF} = \sum_{V_i} \mathbf{f}_{CCF} \Delta V_i, \quad (15)$$

$$\mathbf{T}_{CCF} = \sum_{V_i} (\mathbf{r}_{V_i} \times \mathbf{f}_{CCF}) \Delta V_i, \quad (16)$$

where \mathbf{r}_{V_i} is the distance to the center of the triangular solid surface crossing cell i to the center of rotation of the particle. The force and torque are subsequently passed to the particle motion solver.

In the ideal case of a spherically shaped particle and a stationary spherical droplet, the analytical capillary force from Eq. (11) is given by the total of the line force integration at the contact line dl as

$$\mathbf{F}_{cap,ideal} = 2\pi\sigma R_p \sin a \cos\psi, \quad (17)$$

where R_p is the particle radius, a is the spreading angle from the particle center (see Fig. 1), and ψ is the angle that the interface creates at the

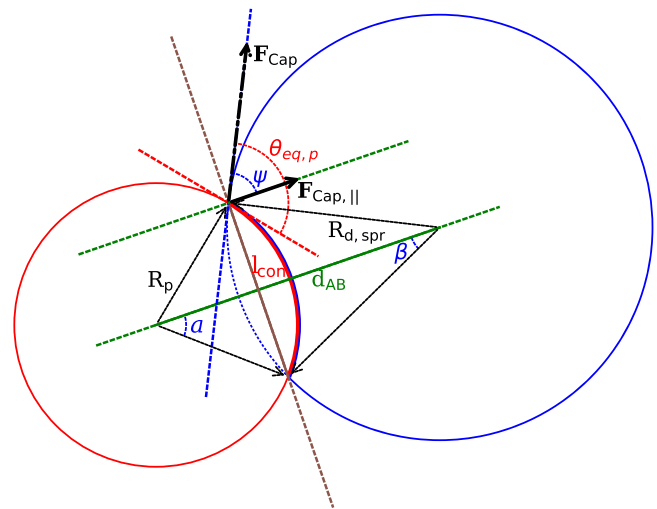


FIG. 1. Geometrical representation of the analytical capillary force in the case of a spherical particle (red circle) and a stationary spherical droplet (blue circle).

contact line with the axis from the centerline of the particle and the droplet. From trigonometry, it is understood that $\psi = \theta_{eq,p} + a - \pi/2$, with $\theta_{eq,p}$ denoting the equilibrium contact angle, given as the average of the advancing and receding contact angles of the particle.

We also needed to develop a method to estimate a possible instantaneous force using the analytical expression and considering the contact line to be fully circular, with a constant contact angle of $\theta_{eq,p}$. To compute the magnitude and direction of this analytical force, the mass center of the droplet is initially computed by our numerical framework by volume averaging. The unit vector $\hat{\mathbf{d}}$ between the two centers is selected to represent the direction of the force. The magnitude is obtained by computing the spreading angle a , and subsequently the angle ψ . To estimate the spreading angle, the contact line position is located in a plane created by $\hat{\mathbf{d}}$ and the z direction unit vector $\hat{\mathbf{e}}_z$. This was performed by evaluating in the investigated plane the liquid volume fraction a in a certain radius R_p from the particle center.

It is important to note that we have observed potential problems when using the CCF model. In particular, when the contact line is experiencing highly dynamic or volatile behavior, and with abrupt retractions and advancements of the contact line on the particle surface, the force \mathbf{F}_{CCF} [Eq. (15)] was unable to capture the anticipated increased attractive forces. To assess the impact of that observation, we have chosen to compare the CCF model (\mathbf{F}_{CCF}) with the analytical expression given in Eq. (17).

By looking at the directions of the two forces, a rather similar behavior was observed, with the CCF force expectedly showcasing a more volatile change, while the analytical formulation capturing the trend well. On the other hand, the magnitudes of the forces showed opposite behaviors with the analytical force attaining local maxima in the same instants that the force from the CCF model showcased local minima. The forces were normalized by the analytical capillary force for an ideal contact area between droplet and particle S_{pl}^* and subsequently also compared with the magnitude of the total hydrodynamic forces acting on the particle [as computed with IBM from Eq. (8)]. The physical explanation for the different trends in the magnitude is at the moment unclear, and a parallel study is undergoing to understand this behavior. Nonetheless, it became apparent to us that the total integrated Laplace pressure force coincided with the weighted average of these two forces, performing exceptionally during all stages of the particle–droplet coalescence and jumping processes. This, and a successful validation against experimental results (shown below), made us comfortable to proceed with our investigation.

For the particle motion, the equations of translation and rotation read

$$m_p \frac{d\mathbf{v}_p}{dt} = \sum_i \mathbf{F}_i = \mathbf{F}_{IB} + \mathbf{F}_{CCF} + \mathbf{F}_{gravity}, \quad (18)$$

$$\mathbf{I} \frac{d\boldsymbol{\omega}_p}{dt} = \sum_i \mathbf{T}_i - \boldsymbol{\omega}_p \times (\mathbf{I} \cdot \boldsymbol{\omega}_p). \quad (19)$$

The computations are provided by a rigid-body dynamics solver with an improved Euler time-stepping scheme. The two equations are solved to obtain the velocity and angular velocity of the particle at the next time step, thereby updating its location in space.

For the immersed boundary, we apply the mirrored immersed boundary method^{40,46} to set the boundary condition for the velocity at the surface. This method estimates the velocity \mathbf{v}_{ghost} for the cells that

are occupied by the solid volume of the object, extrapolating the velocity from a cell in the fluid bulk phase \mathbf{v}_{ext} , along the normal direction of the boundary surface \mathbf{n}_{ds} . The slip velocity \mathbf{v}_{slip} on the boundary is additionally imposed along the tangential direction of the flow $\hat{\mathbf{t}}_C$. The equation reads

$$\frac{\mathbf{v}_{ext} + \mathbf{v}_{ghost}}{2} = \mathbf{v}_{IB} + \mathbf{v}_{slip} \hat{\mathbf{t}}_C, \quad (20)$$

where $\hat{\mathbf{t}}_C$ is given by

$$\hat{\mathbf{t}}_C = \frac{\mathbf{v}_{ext} - (\hat{\mathbf{n}}_C \cdot \mathbf{v}_{ext}) \hat{\mathbf{n}}_C}{\|\mathbf{v}_{ext} - (\hat{\mathbf{n}}_C \cdot \mathbf{v}_{ext}) \hat{\mathbf{n}}_C\|}.$$

For the particle–fluid coupling that requires exchanging of information for the stresses to the rigid-body solver and the updated location and velocity of the particle to the fluid solver, the Newmark time-stepping method⁶¹ is selected.

III. CONFIGURATION OF THE SIMULATION CASES

We describe here how we formulate our simulation cases and obtain fundamental geometrical and dynamical properties of the droplet–particle system. In essence, the numerical setup is based on the experiments performed by Yan *et al.*³⁵ In that study, a spherical particle was positioned on top of a superhydrophobic surface with a droplet, in contact with the substrate, exhibiting spontaneous spreading over the particle. While that study explored particle–droplet coalescence and jumping using three types of particles of various densities and sizes, our investigation focuses on a single particle type that, in our belief, shows the most interesting features of this complex multiphase process. Therefore, we have chosen here to work with the stainless steel particle, which has the highest density of the three particle types in the experiments and is of sufficient size, which facilitates obtaining fine details from the available experimental images.

In all the simulations, the particle has a radius of $R_p = 80 \mu\text{m}$ and is meshed by a volume tetrahedron mesh. In the immersed boundary method (IBM), the surface triangulation is extracted and connected to the Eulerian mesh. The IBM can handle arbitrary shaped objects. We vary the droplet size and define the size ratio k_R as the radius of the particle to the radius of the droplet ($k_R = R_p/R_d$). The domain size and the minimum cell size are selected based on the droplet size, since the curvature of the droplet dictates the capillary-inertial scales of the problem. The size of the computational domain should be large enough to avoid any boundary effects on the droplet–particle system. To be specific, the domain dimensions are set to $10R_d \times 8R_d \times 6R_d$, with the smallest grid size Δx in the vicinity of the interface ranging from 20 to 40 cells per R_d . Additionally, the time step has been adjusted to maintain a constant Courant number $CFL = \|\mathbf{v}\| \Delta t / \Delta x$ for each simulation. The velocity \mathbf{v} in the system is scaled by the capillary-inertial scaling $U_{CI} = \sqrt{\sigma R_d / \rho_l}$. The simulation time t is normalized for the different setups to τ by the capillary-inertial time-scale ($\tau = t / \tau_{CI}$), where τ_{CI} is defined as $\tau_{CI} = \sqrt{\rho_l / (\sigma R_d^3)}$.

To increase computational efficiency, adaptive mesh refinement (AMR) has been employed to maintain the desired refinement near the interface and at the location of the contact line. This allows using coarser resolutions in the regions distant from these critical areas.

The physical properties were defined for a temperature state of 20 °C with the density of air being $\rho_g = 1.204 \text{ kg/m}^3$ and that of the

liquid $\rho_l = 998.21 \text{ kg/m}^3$. The dynamic viscosity of the liquid is set to $\mu_l = 100.16 \times 10^{-5} \text{ Pa s}$ and for the air to $\mu_g = 1.813 \times 10^{-5} \text{ Pa s}$. Finally, the surface tension between air and water has been specified as $\sigma = 7.286 \times 10^{-2} \text{ N/m}$.

The wetting properties of the substrate are first taken in accordance with the experiment. The advancing angle in a static test was recorded as $\theta_{adv,w} = 170.3^\circ$ and the receding one as $\theta_{rec,w} = 167.7^\circ$. Under these conditions, our framework imposes these angles by first establishing from the contact line velocity whether we deal with an advancing or a receding motion. The particle, on the other hand, had a wider range in the measured static contact angles, with the values being between 35° and 76° . Therefore, we have chosen to start with a conservative approach and decided to have an equilibrium contact angle of $\theta_{eq,p} = 55^\circ$ and a static hysteresis of $\Delta\theta_p = 5^\circ$. The advancing and receding angles provided to the system are, thus, $\theta_{adv,p} = 57.5^\circ$ and $\theta_{rec,p} = 52.5^\circ$. In Table I, we summarize the changes that will be introduced as additional simulation cases and as compared to the discussed main configuration (case 1). We vary the droplet size, the wall and particle contact angles, the particle density and, finally, the droplet viscosity. The goal with having those nine additional cases has been to identify and quantify the relative influence of geometrical and wetting droplet, particle, and surface properties on the efficiency of the coalescence and jumping process. We particularly focus on the balances of different components of energy (both the energy beneficial for jumping and that representing losses). Such parameter-related information will be of great relevance when self-cleaning surfaces are to be developed.

To perform a theoretical analysis of the system, we need to define the final contact area between the droplet and the particle, the initial and final interface area between air and droplet, and the initial contact area of the droplet to the substrate. In our problem, the spreading dynamics of the droplet on the particle is governed by the capillary-inertial scales. The ideal spreading area and arch length depend on the radii of the particle and the droplet, as well as on the equilibrium contact angle between the droplet and the particle. The equations to compute the final spreading radius of the droplet $R_{d,spr}$ read as follows:

$$d_{AB} = \sqrt{R_p^2 + R_{d,spr}^2 - 2R_p R_{d,spr} \cos \theta_{eq,p}}, \quad (21)$$

$$\cos a = \frac{R_p^2 + d_{AB}^2 - R_{d,spr}^2}{2R_p d_{AB}}, \quad (22)$$

$$\cos \beta = \sin a \sin \theta_{eq,p} - \cos a \cos \theta_{eq,p}, \quad (23)$$

$$V_{\text{drop,@wall}} = \frac{4}{3}\pi R_d^3 - \frac{1}{3}\pi R_d^3(2 + \cos \theta_{eq,w}) \cdot (1 - \cos \theta_{eq,w})^2, \quad (24)$$

$$V_{\text{part,wet}} = \frac{1}{3}\pi R_p^3(2 + \cos a)(1 - \cos a)^2, \quad (25)$$

$$V_{\text{drop,@part}} = \frac{1}{3}\pi R_{d,spr}^3(2 + \cos \beta)(1 - \cos \beta)^2, \quad (26)$$

$$V_{\text{ideal,@part}} = V_{\text{drop,@wall}} + V_{\text{drop,@part}} + V_{\text{part,wet}}, \quad (27)$$

$$R_{d,spr} = \sqrt[3]{V_{\text{ideal,@part}} / \left(\frac{4}{3}\pi\right)}. \quad (28)$$

The equations presented need to be solved iteratively to determine the apparent radius of the droplet $R_{d,spr}$. In this system of equations, the spreading angles from the center of the particle (a), from the center of the droplet (β), the distance d_{AB} between the spherical centers of the particle and the droplet, and $R_{d,spr}$ represent the unknown variables. For a clearer insight, the reader can visualize the geometric properties of the problem from Fig. 1. Subsequently, the ideal spreading contact area of the system S_{pl}^* is obtained by the following expression, provided the ideal spreading angle a^* was obtained,

$$S_{pl}^* = 2\pi R_p^2(1 - \cos a^*). \quad (29)$$

To estimate the spreading factor β for the cases of liquid spreading on a substrate, most studies use the normalized diameter for the spreading area at the impact duration. We extracted the arch length of the spreading on top of the particle l_{con} to compare with these studies.⁶² The arch length l_{con} is then given from the spreading angle by $l_{con} = 2aR_p$. The spreading length is normalized by the ideal spreading arch length $l_{con}^* = 2a^*R_p$. To compute the instantaneous a , the following expression is required:

TABLE I. List of configurations (cases) for performing numerical simulations of the particle–droplet coalescence and jumping. Note that only the settings changed in relation to the benchmark case (case 1) are presented.

Case No. (-)	Droplet radius R_d (μm)	Substrate θ_{adv} ($^\circ$)	Substrate θ_{rec} ($^\circ$)	Particle θ_{adv} ($^\circ$)	Particle θ_{rec} ($^\circ$)	Particle density ρ_p (kg/m^3)	Liquid dyn. viscosity μ_l (cP)
1	120	170.3	167.7	57.5	52.5	7800	0.100 16
2	240
3	85
4	...	164	158
5	47.5	42.5
6	72.5	67.5
7	62.5	47.5
8	57.5 ^a	52.5 ^a
9	2530	...
10	0.010 016

^aUsing Kistler dynamic contact-angle model.⁵⁵

$$a = \cos^{-1} \left(1 - \frac{S_{pl}}{2\pi R_p^2} \right). \quad (30)$$

According to the literature, the spreading factor β remains constant in a logarithmic scale during the initial spreading phase, which suggests that the spreading dynamics is governed by the velocity of the contact line U_{Cl} .^{63–65} To obtain the spreading factor, a fitting of the arch length is performed in line with the following functional dependence on time $l_{con, norm} \sim \tau^\beta$. Studies in this field^{62,64} suggest that the spreading factor may vary from 0.25 to 0.66, with Yan *et al.*³⁵ estimating it being between 0.40 and 0.70 in the particle–droplet coalescence and jumping case.

Finally, to obtain the energy budget in different simulation cases, the total released surface energy of the system is required. Following the energy analysis in the supplementary material of Yan *et al.*³⁵ and using (i), the Young’s equation $\sigma_{sg} - \sigma_{sl} = \sigma \cos \theta_{eq}$ that connects the specific surface tensions between solid and gas, σ_{sg} , and solid and liquid, σ_{sl} , with the gas–liquid surface tension and the equilibrium contact angle, and (ii) a balance of the contact areas with the solid, such as $S_{sg} = S_{solid} - S_{sl}$ between the solid–gas area S_{sg} , the total solid area S_{solid} and the solid–gas area S_{sg} , we obtain an equation to compute the total released surface energy at any given state in the simulation,

$$\Delta E_{rel, surf} = \sigma (S_{gl}^0 - S_{gl}^f) + \sigma \cos \theta_{eq,p} (S_{pl}^* - S_{pl}^0) - \sigma \cos \theta_{eq,w} S_{wl}^0, \quad (31)$$

where *gl* refers to the air–droplet interface, *pl* is the particle–droplet contact interface, and *wl* is the substrate–droplet interface. The surface energy in the system increases when S_{wl} increases and while the droplet spreads on the superhydrophobic substrate, but after detaching it stops contributing to the energy budget. The indices *0* and *f* denote the initial and final states, respectively.

IV. TIME- AND GRID-CONVERGENCE STUDY AND VALIDATION OF THE SIMULATION FRAMEWORK

The next step in our study is to provide evidence of the temporal and spatial convergence of our numerical framework, and we will start with the former. Within the context of the droplet–particle interaction, a numerical simulation is required to capture the transient spreading of the droplet on the particle. To this end, we selected three time step sizes and compared the resulting spreading dynamics. Throughout each of the simulations, the selected time step remained constant. We choose the initial time step on the basis that the Courant number (CFL) did not exceed 1, peaking slightly above 0.9. The time step was subsequently reduced twice, resulting in the simulations where the CFL remained below 0.5 and 0.25, respectively.

In Fig. 2, we measure the spreading of the droplet on the particle by calculating the arch length l_{con} and comparing it to the ideal spreading length l_{con}^* . The study compares the spreading behavior in a logarithmic scale as a function of normalized time τ . In agreement with prior studies on solid surfaces,^{62,63,66} the spreading follows an exponential growth rate and is governed by inertia. We computed the spreading factor to be 0.366, with all the cases obtaining almost the identical behavior of the spreading length over time. It is in good agreement with the previous experimental results in Yan *et al.*,³⁵ regarding both the spreading time and the spreading factor. The jumping took place at the normalized time of $\tau = 3.25$ for all the cases, and

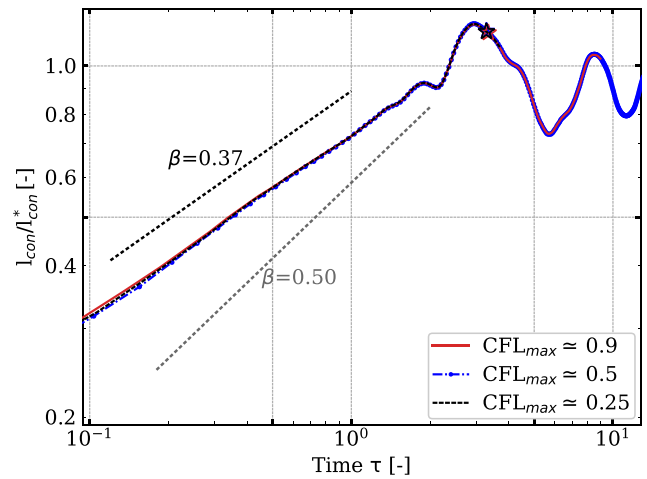


FIG. 2. Time-step independence study comparing the normalized arch lengths of spreading over time. Three different time-steps are evaluated, and we see that the spreading has a constant exponential rate with the spreading factor of $\beta = 0.37$. The asterisk represents the moment of jumping of the droplet–particle system.

it is indicated by an asterisk in the graph. The case with the largest time step with a maximum CFL of a bit more than 0.9 required a higher number of inner SIMPLEC iterations to converge to the residual criterion. For all the cases in this work that will serve for a parametric analysis, we have chosen the median of the three time-steps. The decision is based on our desire to maintain CFL values below 0.5 for the entirety of the simulation, which ensured a continuous behavior of the convective model (CICSAM), enhanced interface sharpness, and reduced the number of inner iterations for convergence.

A grid resolution investigation was also conducted to determine the minimum acceptable cell size Δx , which allows physics-based interface movement and contact line spreading within the particle–droplet–substrate system. We examined three configurations for the cell length at the interface, corresponding to the grid sizes 20, 30, and 40 times smaller than the droplet diameter. The droplet and particle sizes align here with the video images of all stages of the process, provided by Yan *et al.*,³⁵ featuring a particle size of $R_p = 80 \mu\text{m}$, the droplet size of $R_d = 120 \mu\text{m}$, and having the particle–droplet size ratio of $k_R = 0.67$. We have deliberately chosen this setup (with the particle having a relatively high curvature) in order to observe the scales dominated by the droplet pressure jump and the capillary-inertial regime. To this end, the curvature resolution for the particle corresponds to 13.3, 20, and 26.7 cells per particle radius.

To compare the three grid configurations, we examined the calculated different energy components and the obtained trajectories of centers of both particle and the droplet throughout the process. In Fig. 3, we show the energy in the *z* direction, as well as the translational and oscillatory energies for the three different grid sizes, having 20, 30, and 40 cells / R_d . The moment of jumping of the particle–droplet system for each of the grid sizes is indicated with an asterisk. In addition, we tracked the centers of mass of both the particle and the droplet and plotted their locations in the *x*–*z* mid-plane of the system (shown in Fig. 4). We note that the center of the droplet was determined from the volume-averaged center of the liquid volume. The results demonstrate that jumping occurs in all three cases and showcase the

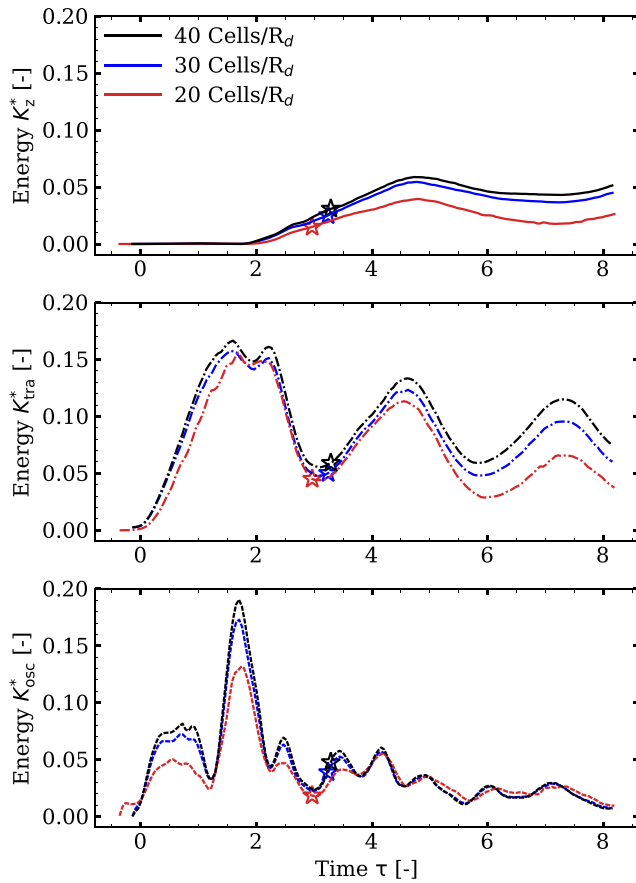


FIG. 3. Different components of energy (in z direction, translational, and oscillatory) for three different grid sizes and with increasingly finer resolutions (from 20 to 40 cells / R_d). The asterisk symbol indicates the moment of particle–droplet jumping in the respective cases.

converging upward motion for the 30 and 40 cell cases, in contrast to the 20 cells / R_d case.

Figure 5 compares the forces acting on the particle. The hydrodynamic forces acting on the surface of the particle (mainly attributed to the higher inner pressure of the droplet on the wetted area, S_{pl}) are compared to the total contact line forces resulting from capillarity. For the three different grid resolutions, a very consistent trend is observed, even though the particle response to these forces exhibits a less converged trajectory. We note that the slight force mismatches between the cases with 30 and 40 cells per radius in Fig. 5 (blue and black line, respectively) will yield a minor inaccuracy for the particle location as the force integrates in time. Therefore, we have chosen the following cornerstones of the grid study, as seen in Fig. 3: the jumping time, the jumping velocity, and the upward energy (which divided by the available energy gives the total efficiency of the process), but also the behavior of the system that is clearly observed in the oscillational part of the kinetic energy. Of course, the displacement, which is a double temporal integration of the acceleration due to the forces acting on the particle, will highlight any small mismatches. We, however, argue that with obtaining so similar velocities for both x and z directions the grid

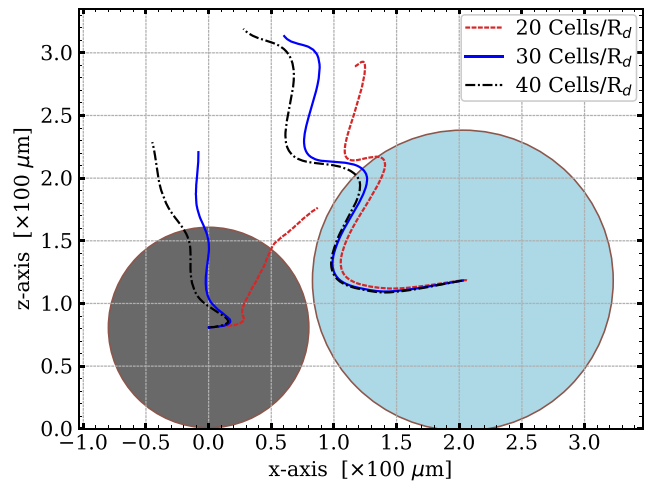


FIG. 4. Trajectories of the centers of the particle (left) and the droplet (right) for three different grid sizes and with increasingly finer resolutions (from 20 to 40 cells per R_d).

validation satisfies the requirements to be able to carry out an extensive investigation of the particle jumping properties. As a result of this analysis, a configuration with 30 cells / R_d is selected for moving forward in our parametric investigation as presented in Sec. V.

Finally, Fig. 6 shows a detailed qualitative comparison between our simulations and a sequence of video snapshots from the

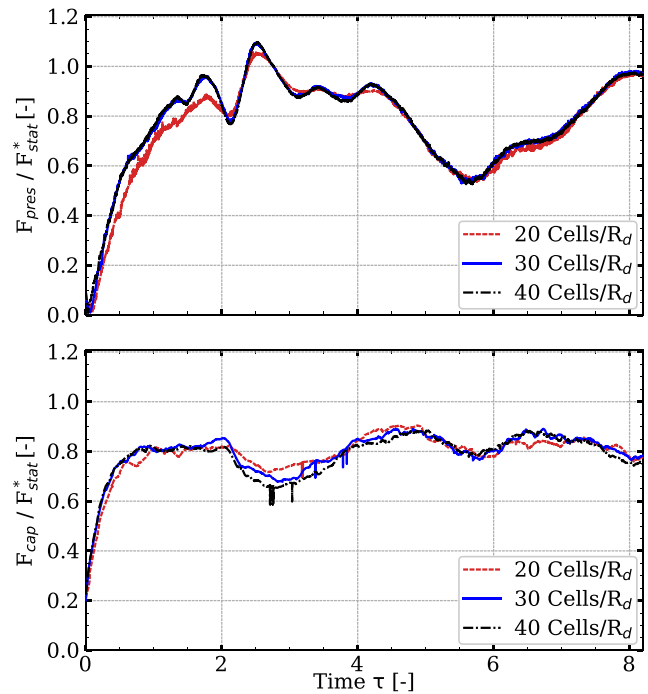


FIG. 5. Computed hydrodynamic forces due to pressure and capillary adhesive forces from our framework (magnitude) for three different grid resolutions. The forces are normalized by the ideal capillary force at rest.

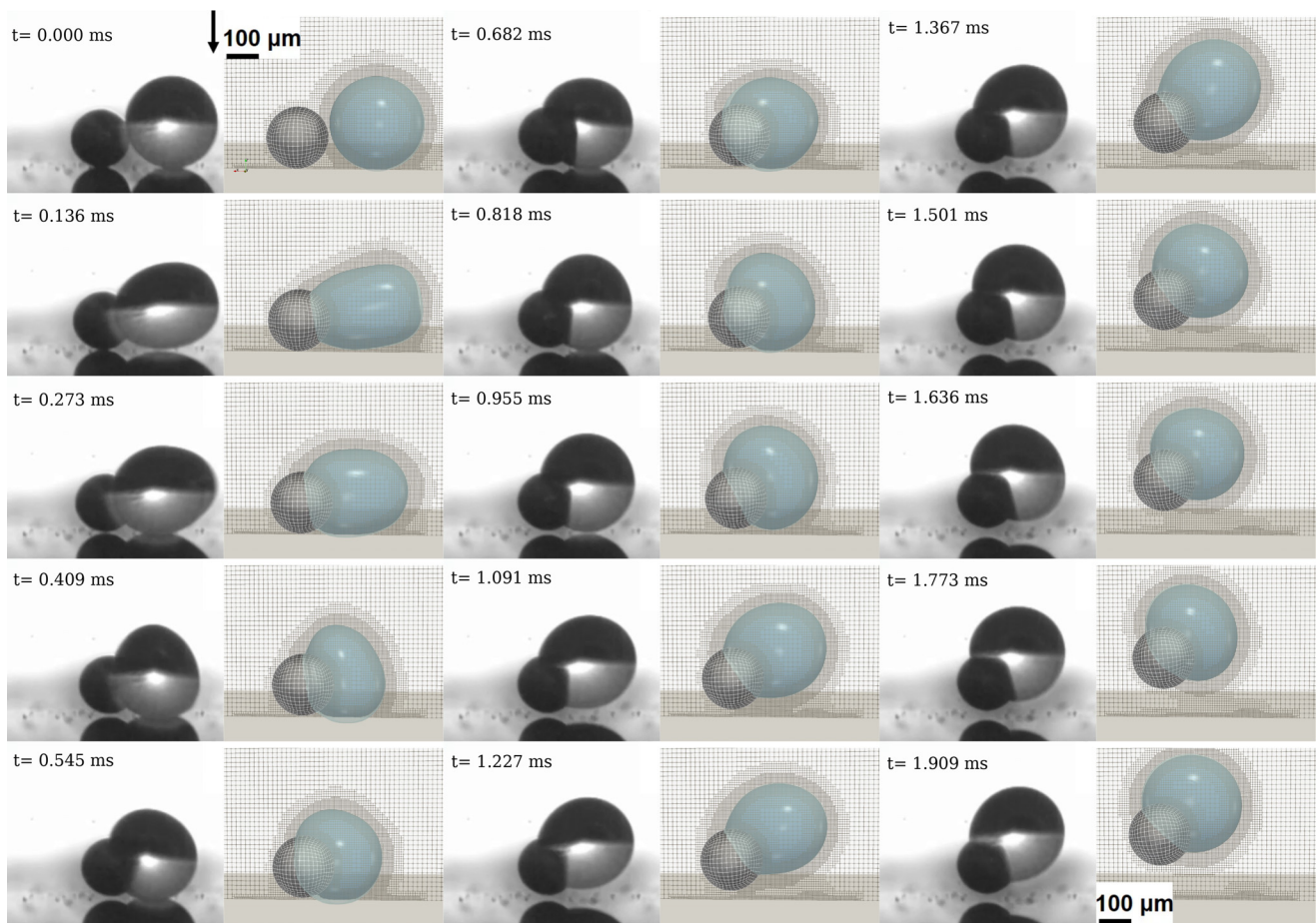


FIG. 6. Comparison between experimentally obtained video images by Yan *et al.*³⁵ (left columns) and our numerical simulation (right columns) for all stages of the droplet–particle coalescence and jumping process. Instants are presented increasing top to bottom, column-wise. The particle radius is $R_p = 80 \mu\text{m}$ (left sphere), and the water droplet radius is $R_d = 120 \mu\text{m}$ (right sphere). The numerical instants match the corresponding experimental ones. We depict the adaptive mesh refinement (AMR). We note a great resemblance of variation of droplet shapes and particle–droplet positions at all instants between the simulations and experiments. The top left image denotes the gravitational vector with a black arrow. Reprinted/adapted with permission from Yan *et al.*, ACS Nano 16, 12910–12921 (2022). Copyright 2022 American Chemical Society.

experiments by Yan *et al.*³⁵ of all stages of the coalescence and jumping process. Overall, we argue that the simulation accurately captures the spreading phase, the propagation of the capillary wave toward the particle, and the entire process of the apparent attraction between the particle and the droplet. We further observe that the oscillations of the droplet, resulting from the movement of the capillary wave, are accurately reproduced. As a result, the developed liquid bridge hits the surface causing a reaction force that is a main mechanism behind the jumping of both the particle and droplet. We acknowledge that the simulated departure shape from the substrate exhibits minimal differences when compared to the experimental images, with the oscillations of the droplet still fully agreeing throughout the process in both types of studies. It is crucial to observe that the moment of departure takes place at the expected instant and that the normalized jumping velocity was $v_{\text{jump}}^* = 0.10$, while Yan *et al.*³⁵ estimated it 0.075. After detachment, the droplet rotates with regard to the particle position (otherwise explained as sliding on the solid surface), with a similar rotational speed as in the experimental images. Finally, a pronounced

disagreement between the two cases is observed during the later stages of the jumping process. We hypothesize that the simulation may incorporate a time-integrated error in the capillary forces, elevating the particle–droplet aggregate with a seemingly higher velocity. In summary, the presented validation makes us comfortable to continue using the developed numerical framework for an analysis of the relative importance of the individual particle and droplet properties on the entire process.

V. RESULTS AND DISCUSSION

We will present and analyze here the results of our simulations by looking at the influence of a chosen system parameter on the outcome of the process. We start by looking at the overall energy budget in the system and continue our analysis with investigating the influence of the chosen particle, droplet, and substrate properties on the identified energy components. These properties can be divided into two groups, and this is how our analysis will be presented: (i) wetting properties of the substrate and the particle and (ii) the droplet and

particle physical properties. The former group comprises the degree of hydrophobicity of the substrate, contact angles at the particle surface (including the influence of hysteresis) and, finally, the effect of implementing a dynamic contact angle model at both the substrate and the particle surface. In the latter group, we look at the influence of changing the droplet size, the particle density (having a significantly lighter particle), and the fluid viscosity.

A. Analysis of the energy budget in the system

Detailed information related to energy budget is essential when assessing the overall efficiency of the particle–droplet coalescence and jumping process. Such information is readily available from our numerical simulations. The available energy of the system stems from the excess surface energy before the droplet initiates spreading on the particle. The surface energy in the particle–droplet contact area minimizes the total energy of the system since our particle is hydrophilic. On the contrary, the surface energy for the area of the droplet in contact with the superhydrophobic substrate increases the total surface energy. When the droplet detaches, the total surface energy of the system is dependent on the particle–droplet area and the droplet–gas interface area. In Fig. 7, the available interface energy is presented for case 1 for all the interfaces in the system. The energy starts from the ideal interface energy measured for starting at rest up to the point when the system jumped and reached an ideal contact area between the particle and the droplet, as computed for the equilibrium contact angle. Moreover, the total kinetic energy of the system (computed from the velocity at each cell of the droplet and the kinetic energy of the particle) is presented. The mentioned plots in the figure are accompanied by those of the total translational kinetic energy computed

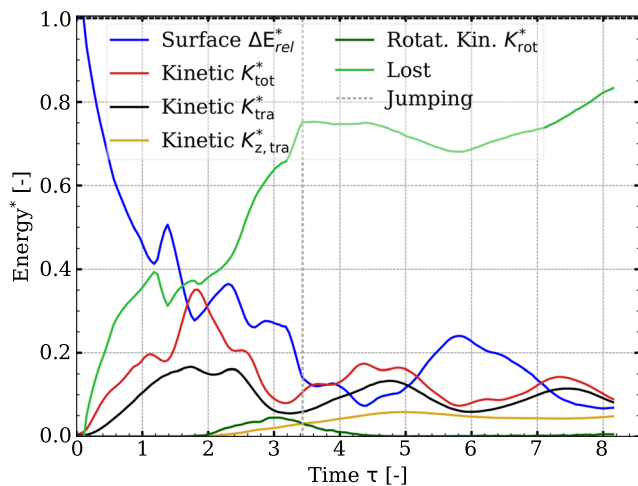


FIG. 7. Energy budget obtained by the simulations for the particle–droplet jumping process, case 1. The decrease in the surface energy normalized by the total available energy in the system is presented in blue. In addition, the total kinetic energy of the system, as well the translational parts for the particles involved, the final translational kinetic energy of the system perpendicular to the substrate (z direction), and the rotational kinetic energy of the system are shown. Finally, we plot the losses in the system as measured by subtracting the available surface energy and the kinetic energies from the total available energy of the system. The vertical dotted gray line denotes the point of droplet–particle departure from the superhydrophobic surface.

from the separate translational kinetic energies of the two bodies, the kinetic energy of the two-body system in the vertical z direction, and the rotational kinetic energy of the system. We observe that the peak kinetic energy of the system reaches roughly 38% of the available energy, while the final gained momentum in the z direction corresponds to approximately 4% of the initial energy. Additionally, the rotation of the system gains energy in the period before detachment, and then, it decreases gradually. When the total kinetic energy of the system is subtracted from the total available energy in the system, we are able to estimate the fraction of the initial energy that is lost either by forms dissipation or by excess contact with the substrate. The latter can indeed be recovered by the system in the form of the kinetic energy, and therefore, the designation of this energy as lost is not necessarily appropriate. Still, we prefer using this term as compared to calling it the dissipated energy. We distinctly observe that the detachment of the droplet from the substrate causes a sudden decrease in the rate of energy being dissipated. After detachment, the energy is lost mostly due to viscosity in the liquid phase or due to contact line movement on the particle surface. Table II gives a summary of the results from the performed simulation cases (following the configurations of Table I), giving the jumping velocity, the total dissipated energy, and the efficiency of the process. An in-depth analysis of these results is included in Secs. VB and VC.

B. Influence of particle and substrate wetting properties

We analyze in this section the effects of different both particle and substrate wetting properties on the overall efficiency of the coalescence and jumping process. In all the cases, we will look at the behavior of different energy components, resulting from variations of the degree of substrate hydrophobicity and the value of the particle surface contact angle hysteresis.

1. Influence of the degree of substrate hydrophobicity

We look here at the effect of the degree of the substrate hydrophobicity on the particle–droplet coalescence and jumping. Superhydrophobic surfaces with high water repellency typically exhibit

TABLE II. Quantified information regarding the jumping velocity, the efficiency of the vertical kinetic energy in relation to the available energy, and the total dissipated energy, as averaged during the last stage of the simulation.

Case No.	Dissipated energy (%)	Jumping velocity norm (-)	Efficiency (%)
1	74.81	0.1079	3.85
2	68.76	0.0780	1.65
3	85.48	0.0514	1.48
4	79.04	0.0799	3.00
5	68.46	0.1523	5.95
6	77.15	0.0966	0.97
7	75.44	0.0442	2.15
8	77.93	0.0674	1.55
9	72.28	0.2260	8.29
10	57.43	0.1040	3.34

15 May 2025 06:35:07

contact angles of 170° and above, while minimizing pinning with a hysteresis of 3° or less. We compare the behavior of the high-performance substrate (case 1), with a second one having a reduced equilibrium contact angle and an increased hysteresis that corresponds to the configuration of case 4 (see Table II). The advancing and receding contact angles selected were 164° and 158° , respectively, presenting a hysteresis of 6° . Our selection is motivated by the minimum possible contact angle that is needed for this case, considering similar values for a classical droplet–droplet coalescence and jumping, that would result in decreased efficiency or even non-jumping. The comparison of the velocities of the two systems is depicted by the evolution of the kinetic energy along the vertical z direction, as shown in Fig. 8. A decrease in that energy is observed for the case with the less superhydrophobic substrate. Additionally, our analysis includes the total translational kinetic energy (adding the rotational energy of the particle) and the oscillating kinetic energy, calculated as the difference between the total kinetic energy accumulated in the system and the translational kinetic energy. Even though there is a minimal difference in the oscillational behavior for the droplet, the translational energy is higher for the high-performance substrate, while the particle–droplet system jumps from

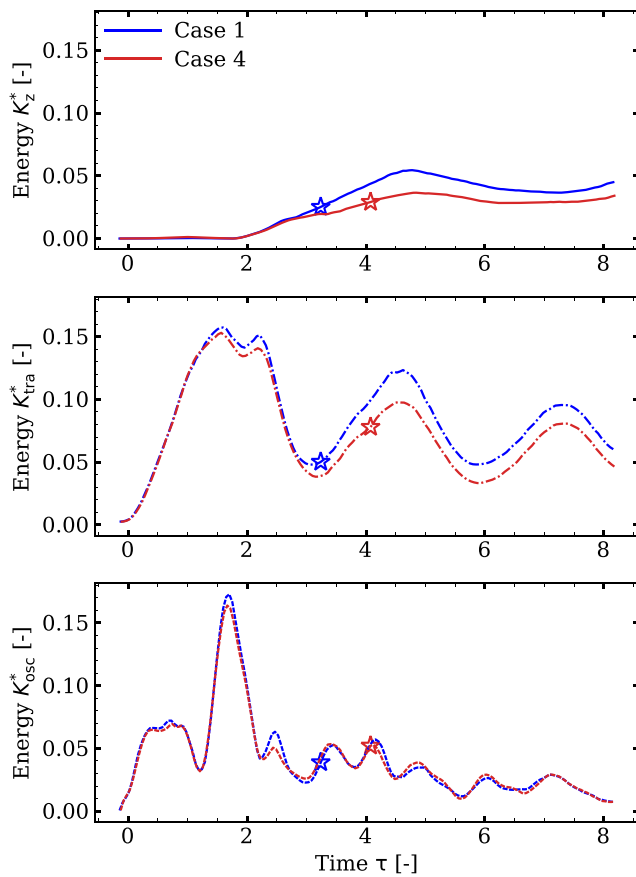


FIG. 8. Influence of the degree of superhydrophobicity of the substrate. We present the kinetic energies in the system for the benchmark case (case 1) and a less superhydrophobic substrate (case 4). The vertical, total translational, and the oscillating ($K_{tot}^* - K_{tra}^*$) energies for the system are normalized by the total released surface energy. The asterisk symbols indicate the moment of jumping.

the surface at an earlier stage (as indicated by an asterisk). These results suggest that further investigation to obtain the minimum contact angle for jumping scenarios requires significant effort involving a wide parameter space, but that it also represents an intriguing topic for future investigations. The parameter space would also be strongly influenced by the particle–droplet size ratio as our previous experimental work suggested.³⁵

2. Influence of the degree of particle hydrophilicity

We know that motion in the system is initiated as the droplet starts spreading on the particle. A decrease in the contact angle with the particle increases the available wetting area on the particle surface. To examine this effect, we simulated two additional cases, with decreased (case 5) and increased (case 6) particle contact angles. From the analysis of the different kinetic energies in the system (Fig. 9), we see that for case 5 with the increased contact area, a higher vertical velocity upon jumping is exhibited. Additionally, a slight delay in

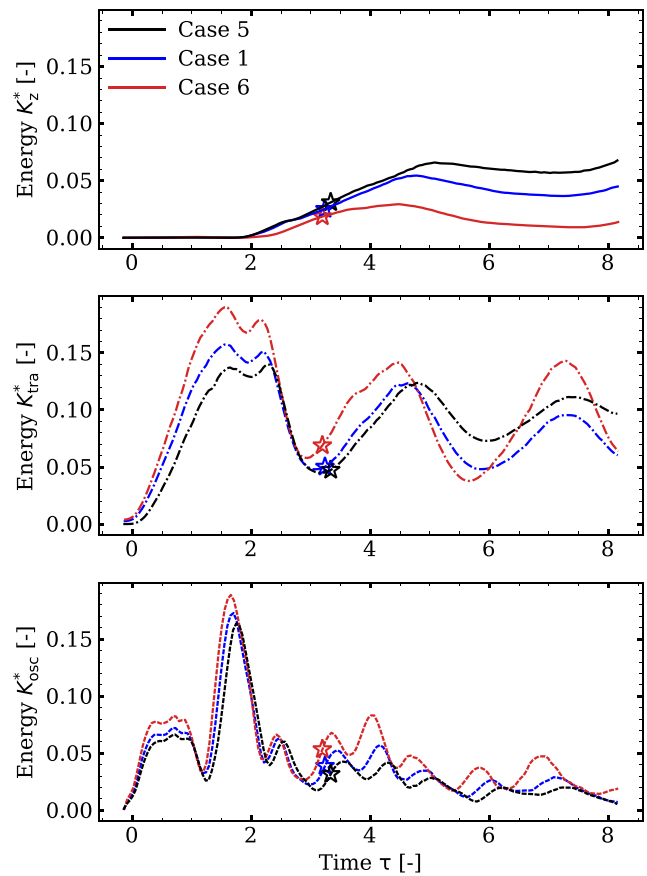


FIG. 9. Influence of the degree of particle hydrophilicity. We plot the kinetic energies in the system for the benchmark case (case 1) and those for the varied contact angles with the particle (cases 5 and 6, where in case 5 we deal with a more hydrophilic particle). We give the vertical, total translational, and the oscillating energies for the system normalized by the total released surface energy. Using lower particle contact angles results in the higher percentage of the released energy that is turned to vertical momentum. The asterisk symbols indicate the moment of jumping.

15 May 2025 06:35:07

reaction is recorded until the maximum spreading and jumping. The data, seen also in Table II, suggest that the non-normalized values for the total kinetic energy increase when the contact angle is reduced. This is expected due to the greater forces and the available wetting area. However, for the normalized kinetic energies presented in Fig. 9, we observe a slight decrease in the total translational (and rotational for the particle) kinetic energy for $\theta_{eq} = 45^\circ$. This effect is attributed to the increase in the available surface energy when the equilibrium contact angle on the particle decreases. Therefore, the rate of transformed energy into the total kinetic energy decreases when the particle has a larger contact area with the droplet. We consider this to be the result of the higher dissipation near the contact line, as both the area and the contact line increase in size. In contrast, the upward momentum of the system becomes higher, so even if a fraction of the energy is to be absorbed into the kinetic energy, there is still enough excess surface energy and a greater contact area with the substrate, causing the particle-droplet system to jump with more energy. We present in Fig. 10 the increase in the maximum contact area between the particle and the droplet due to the decreasing contact angles.

3. Influence of the degree of particle surface hysteresis and of employing a dynamic contact angle model

Next, we investigate the influence of different degrees of hysteresis on the particle surface, again focusing on the energy balance for the system. Emphasis is placed on quantifying the percentage of the energy that is lost due to dissipation when the droplet is experiencing a higher degree of hysteresis with the particle. Hysteresis, being defined as the difference between the angles observed in advancing and receding motions of the contact line, can be represented in the framework in two ways. The first one is by prescribing a constant degree of hysteresis or, alternatively, by varying the exact values of the contact angle imposed for the two different motions. The second way to estimate the influence of particle contact angles is by obtaining the effective contact

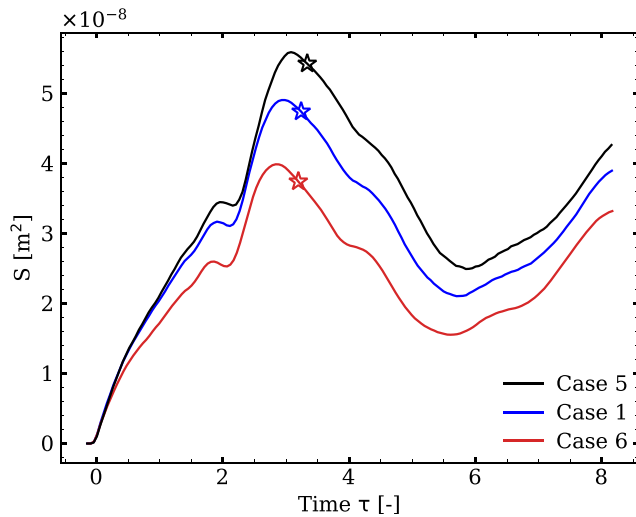


FIG. 10. Contact areas measured on the particle surface obtained by the simulations for cases 1 (the benchmark case), 5 and 6, treating particles with the different degree of hydrophilicity. Case 5 involves a more hydrophilic particle.

angle from a dynamic contact-angle model. In our study, we utilize the Kistler dynamic model,^{55–57} where the value for the contact angle is dependent on the contact line velocity. The model requires the advancing and receding contact angles as an input, as they are observed from a static experimental configuration. For a setup with a static hysteresis of 5° , equivalent to the low hysteresis configuration for the benchmark case (case 1), the effective hysteresis for the simulation that corresponds to case 8 is measured to be 15° . Therefore, the described case provides a suitable comparison with a setup that imposes a constant hysteresis of 15° and using the quasi-static model (case 7).

The kinetic energy in the vertical direction is decreased for the cases with a more pronounced hysteresis, as depicted in Fig. 11. Furthermore, the total translational kinetic energy in the system has also decreased, both for the higher hysteresis with the static angles case and the one with the dynamic contact-angle model. The percentage of

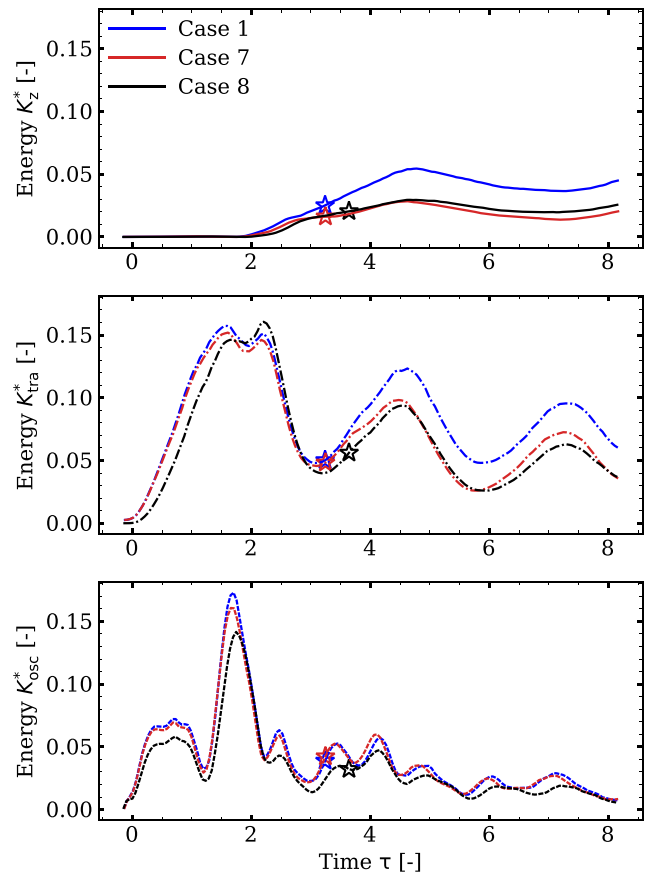


FIG. 11. Influence of the degree of particle surface hysteresis and of using a dynamic contact-angle model. We plot the different kinetic energies for case 7 (a higher degree of hysteresis and with the quasi-static representation for contact angles) and case 8 (using the Kistler dynamic contact-angle model) and compare with those in the benchmark case (case 1) that uses a quasi-static representation but with a moderate degree of hysteresis. The vertical, total translational, and the oscillating energy components for the system are normalized by the total released surface energy. With a higher degree of hysteresis, the jumping efficiency decreases and the kinetic energy shows a more pronounced dissipation. The asterisk symbols indicate the moment of jumping.

15 May 2025 06:35:07

the decrease is consistent for the two simulations, indicating that having a higher hysteresis, mostly due to a greater advancing angle, results in increased losses in the system after jumping. The jumping in the non-benchmark cases takes place moments after that in the benchmark case (case 1), as indicated by an asterisk in the respective cases. Case 7 with static hysteresis jumps after the benchmark case, with the Kistler case 8 detaching slightly afterward. Finally, the energy from the droplet oscillations appears to have slightly decreased for the dynamic model case, without affecting the kinetic energy saved in the system, while the static hysteresis case of 15° turns nearly identical to the benchmark case (case 1). Our analysis suggests that for the simulations that aim to more accurately estimate dissipation stemming from the particle surface hysteresis, precise values are required for the advancing and receding contact angles. Such values may be recorded in a dynamic test. For the cases with high effective hysteresis, using a dynamic contact-angle model can be a better option, especially if exact values of the angles cannot be provided. In this work, the benchmark case (case 1) has been designed having a low degree of hysteresis, since the information on the angles in the experimental tests varied significantly. Therefore, the effect of hysteresis is otherwise neglected in further investigations.

C. Influence of the droplet and particle physical properties

We will here investigate again the variation of different energy components, but this time as a function of changing the droplet and particle physical properties. We start with the effect of changing the droplet size and continue the analysis with working with a lighter particle and having a less viscous liquid phase in the system.

1. Influence of the droplet size

Experiments of Yan *et al.*³⁵ have shown that different types of particles required different particle–droplet size ratios to achieve efficient jumping and attain higher jumping velocities. For the stainless steel particle, we are working with in our simulations, and this ratio is $k_r \simeq 0.6$, with the maximum normalized jumping velocity of 0.09.³⁵ We have chosen to test a larger droplet with the radius of $240 \mu\text{m}$ for case 2 (from the $120 \mu\text{m}$ radius of the benchmark case 1) and a smaller with an $85 \mu\text{m}$ radius defining case 3 in our study. Such a change influences the characteristic capillary-inertial velocity and time scales of the system. From the process efficiency table (Table II), it is observed that the normalized jumping velocity for the benchmark case (case 1) is 0.11, with its values being reduced to 0.8 and 0.5 for the larger (case 2) and the smaller droplet size (case 3), respectively. The kinetic energy in the z direction, as shown in Fig. 12, demonstrates a notable increase in the velocity in the early stage of coalescing for the larger droplet case. We attribute this effect to the stronger capillary forces attracting the particle toward the droplet with an energy component in the z direction, as well as due to the particle–droplet size mismatch. Since in case 2, the Laplace pressure decreases, the effect of the attracting force becomes stronger during the spreading phase. This energy is primarily transferred to the particle, with the droplet displacing at a later stage. Additionally, the increased inertia forces are evident from the oscillatory kinetic energy of the system, as the oscillations in the droplet are not dampened for the duration of the simulation. The total kinetic energy of the system displays a volatile behavior, with dissimilar time

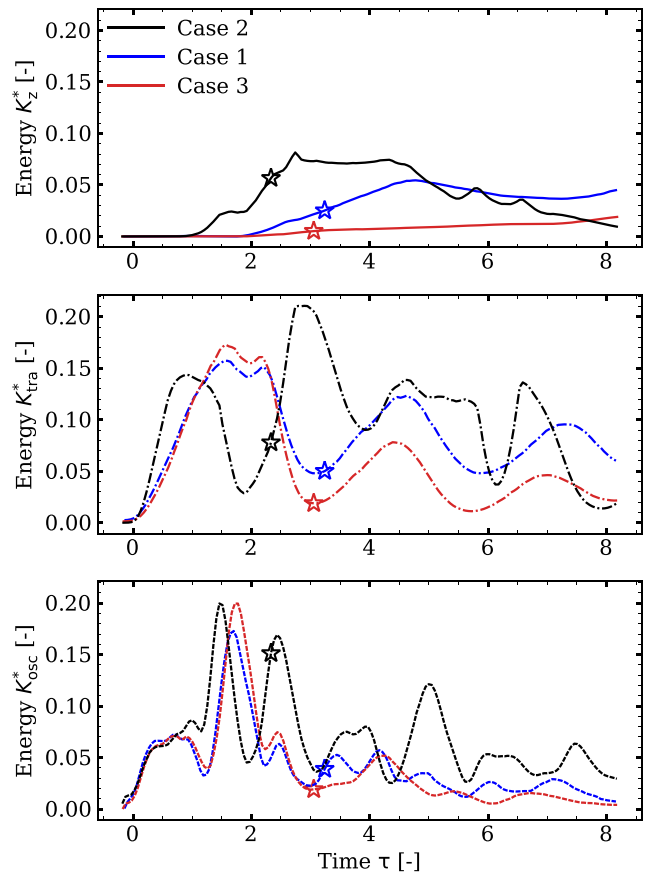


FIG. 12. Influence of the variation of the droplet size. We plot the kinetic energies for the droplet sizes of $R_d = 120, 240$, and $85 \mu\text{m}$, corresponding to cases 1, 2, and 3, respectively. We show the vertical, total translational, and the oscillating kinetic energies normalized by the total released surface energy. The largest droplet attracts the particle differently from the other two droplets and achieves detachment earlier, but with a lower velocity. The smallest droplet shows a higher dissipation rate and exhibits less efficient jumping. The moment of jumping in all the cases is indicated by an asterisk.

scales for maximum spreading and jumping. Furthermore, the particle–droplet system experiences in this case only a slight elevation and retains a minimal upward velocity. On the other hand, the smaller droplet (case 3) retains the same trends for jumping as the benchmark case (case 1), albeit with a significantly reduced jumping velocity. The oscillations are now dampened earlier due to the higher dissipation present in that configuration. Notably, the efficiency of the translational kinetic energy decreases for both the smaller and the larger droplet, aligning with the experimental findings from Yan *et al.*³⁵

2. Influence of particle density

The particle density significantly influences the particle response to the forces acting on it, since the density proportionally changes the momentum of the particle. We test here the behavior of a lighter particle with the density of 2530 kg/m^3 (case 9), corresponding to the soda-lime glass particle of the experimental study by Yan *et al.*³⁵ We keep

the remaining parameters (contact angles and size) consistent with the benchmark case (case 1). Figure 13 displays the normalized kinetic energies of the system. The results suggest that the contact angles and the droplet size are indeed the primary factors influencing the oscillations in the droplet. The rationale behind this observation is that we could not observe significant differences between cases 1 and 9. However, less total translational energy is observed in the system in the latter case, clearly due to the decreased mass of the particle. The main conclusion from these results is that the peak upward velocity for the particle–droplet system increases significantly, achieving more than a doubled efficiency for the jumping process compared with the benchmark case (exceeding 8%, see case 9 in Table II).

3. Influence of viscosity of the liquid phase

Having noted variations in the dissipation with changes in the droplet size and capillary-inertial scales, we investigated how the change of the liquid-phase viscosity affects the particle–droplet

coalescence and jumping. We now define case 10 by reducing this viscosity to one tenth of that in the benchmark case (case 1), which corresponds to a decrease in the characteristic Ohnesorge number from 0.0107 to 0.00107. Although the maximum spreading area remains constant, oscillations in the contact line persist longer. Figure 14 compares the kinetic energies of the system. As expected, the wave-like behavior of the translational kinetic energy persists with a higher amplitude and less energy losses over time compared to those in case 1. This outcome clearly suggests that there is less viscous dissipation in the later stage of the process, where the droplet detaches from the substrate. The vertical velocity is also increased throughout the simulation, indicating a minimized viscous dissipation at the particle surface and near the contact line. Moreover, the higher inertia in the system causes the energy stored by oscillations from the droplet to remain constant during the airborne stage of the simulation.

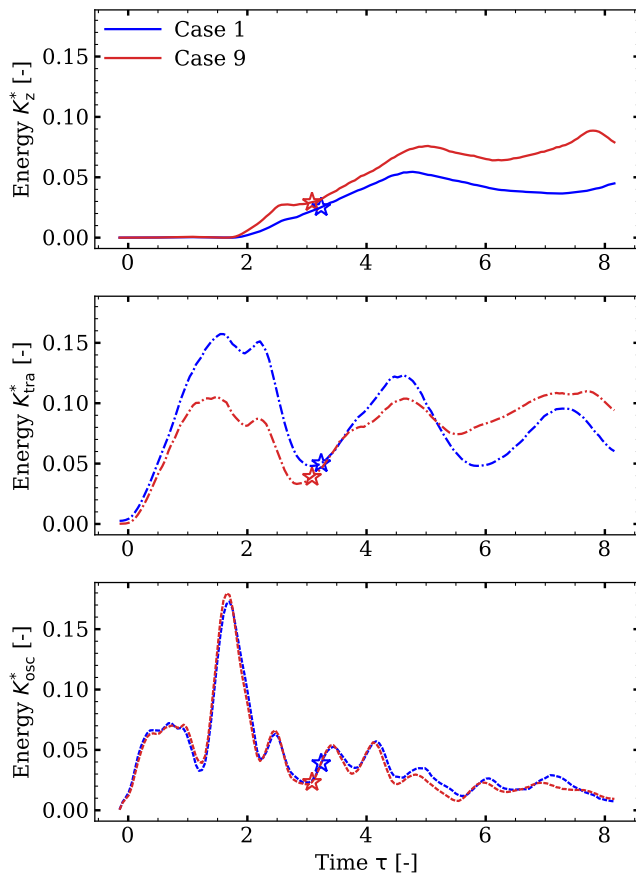


FIG. 13. Influence of the variation of particle density. We plot different components of the kinetic energy for a soda-lime glass particle ($\rho_p = 2530 \text{ kg/m}^3$) of case 9 and compare with those involving a heavy stainless steel particle ($\rho_p = 7800 \text{ kg/m}^3$) of case 1. The light particle is propelled by the droplet motion with a higher velocity, even though less kinetic energy is absorbed by the system. The moment of jumping is indicated by an asterisk in the respective cases.

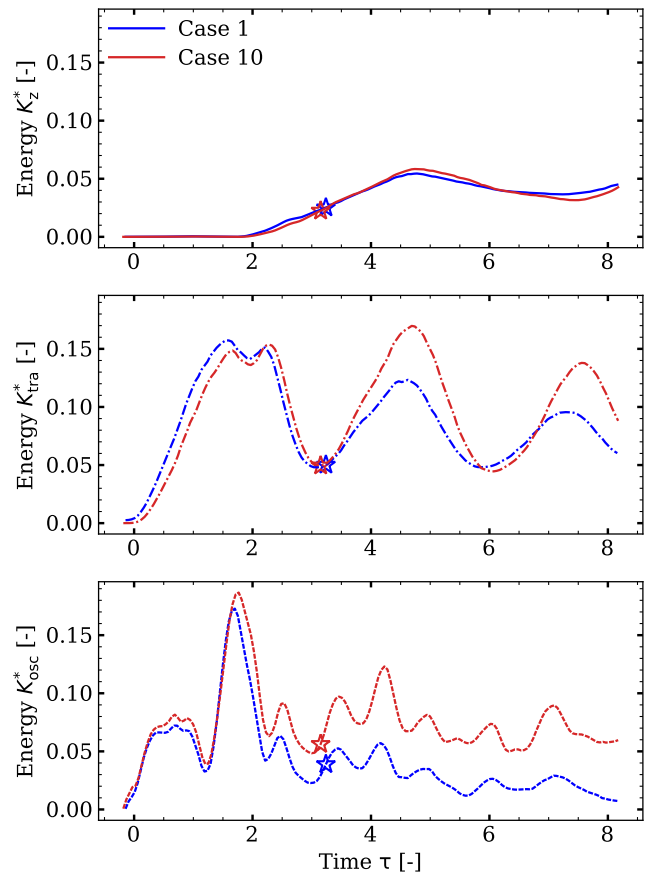


FIG. 14. Influence of the liquid-phase viscosity. We plot different components of the kinetic energy for the simulations with variable liquid-phase viscosities. In the benchmark case (case 1), the viscosity is ten times higher in comparison with that of case 10. From the vertical, total translational and oscillating kinetic energies—normalized by the total released surface energy—we note the relevance of viscosity for the system behavior after jumping. The jumping velocity remains the same, but the oscillations in the droplet and the translational kinetic energy are stronger and more persistent in the low viscosity case. The moment of jumping is indicated by an asterisk in the respective cases.

15 May 2025 06:35:07

VI. CONCLUSIONS

We have performed a comprehensive multiphase direct numerical study (using a combined VOF—immersed boundary method) of coalescence and subsequent jumping from a superhydrophobic surface of a particle–single droplet system. Our simulations reveal fundamental dynamics of all relevant stages of that passive self-cleaning mechanism for the removal of contaminants from surfaces in both nature and technological applications: (i) initial spreading of the droplet on the particle (and development of a liquid bridge), (ii) oscillation of the droplet normal to the surface and the impact of the liquid bridge to the surface, and (iii) departure of the particle–droplet system from the surface. A thorough validation demonstrated temporal and spatial convergence of the developed numerical framework. A fully resolved three-dimensional simulation was compared with the previously published experimental images,³⁵ with great agreement in capturing the overall droplet–particle behavior and good conformity related to the removal of the particle from the substrate due to the capillary forces acting at the three-phase contact line. We have implemented a model for the estimation of capillary forces from a continuum perspective⁵⁹ and introduced our suggestions on how to reduce oscillations of the adhesion forces in a multiphase direct numerical simulations (DNS) framework.

We have systematically investigated particle-, droplet- and surface wetting, and geometrical properties and their influence on the coalescence and jumping processes. In the chosen parameter space, we have quantified energy efficiencies and dissipation, information that is not straightforward to elucidate from experiments. We have shown that pronounced superhydrophobicity enhances the efficiency of the jumping process, while the average contact angle at the particle surface is of great significance for the available energy and the dynamics of the process. We demonstrate an increase in dissipation when both higher degrees of hysteresis at the particle surface are present and when the viscosity of the droplet is increased. The simulations prove that the size of the droplet is an important parameter, with an increasing dissipation when the size of the droplet tends to that of the particle.

Our particle properties (wettability, size, and density) are representative of typical deposits on many outdoor surfaces in nature and industrial applications. The findings of this study thus provide guidelines for the design of functional surfaces for various technological applications.

ACKNOWLEDGMENTS

The authors would like to acknowledge the Swedish Research Council for the financial support of this project (Vetenskapsrådet, No. 2019-04969). In addition, we would like to acknowledge that the handling of data and other computations were enabled by resources provided by the National Academic Infrastructure for Supercomputing in Sweden (NAISS), partially funded by the Swedish Research Council through Grant Agreement No. 2022-06725.

AUTHOR DECLARATIONS

Conflict of Interest

The authors have no conflicts to disclose.

Author Contributions

K. Konstantinidis: Conceptualization (equal); Data curation (equal); Formal analysis (equal); Methodology (equal); Software (equal);

Validation (equal); Visualization (equal); Writing – original draft (equal); Writing – review & editing (equal). **J. Göhl:** Formal analysis (equal); Investigation (equal); Methodology (equal); Software (equal); Validation (equal); Visualization (supporting); Writing – review & editing (equal). **A. Mark:** Formal analysis (supporting); Funding acquisition (supporting); Investigation (equal); Methodology (equal); Resources (equal); Software (lead); Supervision (equal); Validation (equal); Visualization (supporting); Writing – review & editing (equal). **X. Yan:** Formal analysis (equal); Investigation (equal); Resources (equal); Validation (equal); Visualization (supporting); Writing – review & editing (equal). **N. Miljkovic:** Formal analysis (equal); Investigation (equal); Resources (equal); Validation (equal); Visualization (supporting); Writing – review & editing (equal). **S. Sasic:** Conceptualization (equal); Formal analysis (equal); Funding acquisition (equal); Investigation (equal); Methodology (equal); Project administration (equal); Resources (equal); Supervision (equal); Validation (equal); Visualization (equal); Writing – review & editing (equal).

DATA AVAILABILITY

The data that support the findings of this study are available from the corresponding author upon request.

REFERENCES

- Q. Hao, Y. Pang, Y. Zhao, J. Zhang, J. Feng, and S. Yao, “Mechanism of delayed frost growth on superhydrophobic surfaces with jumping condensates: More than interdrop freezing,” *Langmuir* **30**, 15416–15422 (2014).
- F. Chu, Y. Lin, X. Yan, and X. Wu, “Quantitative relations between droplet jumping and anti-frosting effect on superhydrophobic surfaces,” *Energy Build.* **225**, 110315 (2020).
- J. Ma, S. Sett, H. Cha, X. Yan, and N. Miljkovic, “Recent developments, challenges, and pathways to stable dropwise condensation: A perspective,” *Appl. Phys. Lett.* **116**, 260501 (2020).
- W. Barthlott and C. Neinhuis, “Purity of the sacred lotus, or escape from contamination in biological surfaces,” *Planta* **202**, 1–8 (1997).
- K. S. Boyina, A. J. Mahvi, S. Chavan, D. Park, K. Kumar, M. Lira, Y. Yu, A. A. Gunay, X. Wang, and N. Miljkovic, “Condensation frosting on meter-scale superhydrophobic and superhydrophilic heat exchangers,” *Int. J. Heat Mass Transfer* **145**, 118694 (2019).
- J. Oh, C. E. Dana, S. Hong, J. K. Román, K. D. Jo, J. W. Hong, J. Nguyen, D. M. Cropek, M. Alleyne, and N. Miljkovic, “Exploring the role of habitat on the wettability of cicada wings,” *ACS Appl. Mater. Interfaces* **9**, 27173–27184 (2017).
- T. Wagner, C. Neinhuis, and W. Barthlott, “Wettability and contaminability of insect wings as a function of their surface sculptures,” *Acta Zool.* **77**, 213–225 (1996).
- P. Roach, N. J. Shirtcliffe, and M. I. Newton, “Progress in superhydrophobic surface development,” *Soft Matter* **4**, 224 (2008).
- X. Yan, Z. Huang, S. Sett, J. Oh, H. Cha, L. Li, L. Feng, Y. Wu, C. Zhao, D. Orejon, F. Chen, and N. Miljkovic, “Atmosphere-mediated superhydrophobicity of rationally designed micro/nanostructured surfaces,” *ACS Nano* **13**, 4160–4173 (2019).
- C. W. Yao, S. Tang, D. Sebastian, and R. Tadmor, “Sliding of water droplets on micropillar-structured superhydrophobic surfaces,” *Appl. Surf. Sci.* **504**, 144493 (2020).
- X. Yan, L. Zhang, S. Sett, L. Feng, C. Zhao, Z. Huang, H. Vahabi, A. K. Kota, F. Chen, and N. Miljkovic, “Droplet jumping: Effects of droplet size, surface structure, pinning, and liquid properties,” *ACS Nano* **13**, 1309–1323 (2019).
- D. Wang, Q. Sun, M. J. Hokkanen, C. Zhang, F. Y. Lin, Q. Liu, S. P. Zhu, T. Zhou, Q. Chang, B. He, Q. Zhou, L. Chen, Z. Wang, R. H. Ras, and X. Deng, “Design of robust superhydrophobic surfaces,” *Nature* **582**, 55–59 (2020).

- ¹³J. Xie, J. Xu, X. Li, and H. Liu, "Dropwise condensation on superhydrophobic nanostructure surface, Part I: Long-term operation and nanostructure failure," *Int. J. Heat Mass Transfer* **129**, 86–95 (2019).
- ¹⁴S. F. Zheng, U. Gross, and X. D. Wang, "Dropwise condensation: From fundamentals of wetting, nucleation, and droplet mobility to performance improvement by advanced functional surfaces," *Adv. Colloid Interface Sci.* **295**, 102503 (2021).
- ¹⁵H. Wang, L. Tang, X. Wu, W. Dai, and Y. Qiu, "Fabrication and anti-frosting performance of super hydrophobic coating based on modified nano-sized calcium carbonate and ordinary polyacrylate," *Appl. Surf. Sci.* **253**, 8818–8824 (2007).
- ¹⁶A. Guha, "Transport and deposition of particles in turbulent and laminar flow," *Annu. Rev. Fluid Mech.* **40**, 311–341 (2008).
- ¹⁷C. Yu, S. Sasic, K. Liu, S. Salameh, R. H. Ras, and J. R. van Ommen, "Nature-inspired self-cleaning surfaces: Mechanisms, modelling, and manufacturing," *Chem. Eng. Res. Des.* **155**, 48–65 (2020).
- ¹⁸J. B. Boreyko and C. H. Chen, "Self-propelled dropwise condensate on superhydrophobic surfaces," *Phys. Rev. Lett.* **103**, 184501 (2009).
- ¹⁹F. Liu, G. Ghigliotti, J. J. Feng, and C.-H. Chen, "Numerical simulations of self-propelled jumping upon drop coalescence on non-wetting surfaces," *J. Fluid Mech.* **752**, 39–65 (2014).
- ²⁰K. M. Wisdom, J. A. Watson, X. Qu, F. Liu, G. S. Watson, and C.-H. Chen, "Self-cleaning of superhydrophobic surfaces by self-propelled jumping condensate," *Proc. Natl. Acad. Sci. U. S. A.* **110**, 7992–7997 (2013).
- ²¹R. Enright, N. Miljkovic, J. Sprittles, K. Nolan, R. Mitchell, and E. N. Wang, "How coalescing droplets jump," *ACS Nano* **8**, 10352–10362 (2014).
- ²²R. Mukherjee, H. A. Gruszewski, L. T. Bilyeu, D. G. Schmale, and J. B. Boreyko, "Synergistic dispersal of plant pathogen spores by jumping-droplet condensation and wind," *Proc. Natl. Acad. Sci. U. S. A.* **118**, e2106938118 (2021).
- ²³Y. Li, H. Zhang, J. Du, Q. Min, X. Wu, and L. Sun, "Coalescence-induced self-propelled particle transport with asymmetry arrangement," *ACS Appl. Mater. Interfaces* **16**, 18184 (2024).
- ²⁴J. Tian, J. Zhu, H. Y. Guo, J. Li, X. Q. Feng, and X. Gao, "Efficient self-propelling of small-scale condensed microdrops by closely packed ZnO nano-needles," *J. Phys. Chem. Lett.* **5**, 2084–2088 (2014).
- ²⁵Z. Yuan, X. Wu, F. Chu, and R. Wu, "Numerical simulations of guided self-propelled jumping of droplets on a wettability gradient surface," *Appl. Therm. Eng.* **156**, 524–530 (2019).
- ²⁶S. Li, F. Chu, J. Zhang, D. Brutin, and D. Wen, "Droplet jumping induced by coalescence of a moving droplet and a static one: Effect of initial velocity," *Chem. Eng. Sci.* **211**, 115252 (2020).
- ²⁷F. Chu, S. Li, Z. Ni, and D. Wen, "Departure velocity of rolling droplet jumping," *Langmuir* **36**, 3713–3719 (2020).
- ²⁸F. Chu, X. Yan, and N. Miljkovic, "How superhydrophobic grooves drive single-droplet jumping," *Langmuir* **38**, 4452–4460 (2022).
- ²⁹N. Miljkovic, R. Enright, and E. N. Wang, "Effect of droplet morphology on growth dynamics and heat transfer during condensation on superhydrophobic nanostructured surfaces," *ACS Nano* **6**, 1776–1785 (2012).
- ³⁰R. Attarzadeh and A. Dolatabadi, "Coalescence-induced jumping of microdroplets on heterogeneous superhydrophobic surfaces," *Phys. Fluids* **29**, 012104 (2017).
- ³¹R. Mukherjee, A. S. Berrier, K. R. Murphy, J. R. Veitez, and J. B. Boreyko, "How surface orientation affects jumping-droplet condensation," *Joule* **3**, 1360–1376 (2019).
- ³²K. Konstantinidis, J. Göhl, A. Mark, and S. Sasic, "Coalescence-induced jumping of droplets from superhydrophobic surfaces—The effect of contact-angle hysteresis," *Phys. Fluids* **34**, 113302 (2022).
- ³³S. Farokhirad and T. Lee, "Computational study of microparticle effect on self-propelled jumping of droplets from superhydrophobic substrates," *Int. J. Multiphase Flow* **95**, 220–234 (2017).
- ³⁴K. W. Connington, T. Lee, and J. F. Morris, "Interaction of fluid interfaces with immersed solid particles using the lattice Boltzmann method for liquid-gas-particle systems," *J. Comput. Phys.* **283**, 453–477 (2015).
- ³⁵X. Yan, B. Ji, L. Feng, X. Wang, D. Yang, K. F. Rabbi, Q. Peng, M. J. Hoque, P. Jin, E. Bello, S. Sett, M. Alleyne, D. M. Crokek, and N. Miljkovic, "Particulate-droplet coalescence and self-transport on superhydrophobic surfaces," *ACS Nano* **16**, 12910–12921 (2022).
- ³⁶M. Preuss and H. J. Butt, "Measuring the contact angle of individual colloidal particles," *J. Colloid Interface Sci.* **208**, 468–477 (1998).
- ³⁷A. Amirfazli and A. W. Neumann, "Status of the three-phase line tension: A review," *Adv. Colloid Interface Sci.* **110**, 121–141 (2004).
- ³⁸P. A. Kralchevsky and K. Nagayama, "Capillary interactions between particles bound to interfaces, liquid films and biomembranes," *Adv. Colloid Interface Sci.* **85**, 145–192 (2000).
- ³⁹B. Andreotti and J. H. Snoeijer, "Statics and dynamics of soft wetting," *Annu. Rev. Fluid Mech.* **52**, 285–308 (2020).
- ⁴⁰A. Mark and B. G. van Wachem, "Derivation and validation of a novel implicit second-order accurate immersed boundary method," *J. Comput. Phys.* **227**, 6660–6680 (2008).
- ⁴¹H. V. Patel, S. Das, J. A. Kuipers, J. T. Padding, and E. A. Peters, "A coupled volume of fluid and immersed boundary method for simulating 3D multiphase flows with contact line dynamics in complex geometries," *Chem. Eng. Sci.* **166**, 28–41 (2017).
- ⁴²A. O'Brien and M. Bussmann, "A volume-of-fluid ghost-cell immersed boundary method for multiphase flows with contact line dynamics," *Comput. Fluids* **165**, 43–53 (2018).
- ⁴³A. O'Brien and M. Bussmann, "A moving immersed boundary method for simulating particle interactions at fluid-fluid interfaces," *J. Comput. Phys.* **402**, 109089 (2020).
- ⁴⁴M. Saeedipour, A. Nair, and S. Pirker, "A coupled volume of fluid-fictitious domain method to study droplet-particle interactions at different impact conditions," in *ICLASS, 2021 15th Triennial International Conference on Liquid Atomization and Spray Systems, Edinburgh, UK, 29 August-2 September 2021* (ICLASS, 2021).
- ⁴⁵K. Washino, E. L. Chan, T. Tsujimoto, T. Tsuji, and T. Tanaka, "Development of resolved CFD-DEM coupling method for three-phase flows with non-spherical particles," *Chem. Eng. Sci.* **267**, 118335 (2023).
- ⁴⁶A. Mark, R. Rundqvist, and F. Edvelik, "Comparison between different immersed boundary conditions for simulation of complex fluid flows," *Fluid Dyn. Mater. Process.* **7**, 241–258 (2011).
- ⁴⁷J. P. Van Doormaal and G. D. Raithby, "Enhancements of the simple method for predicting incompressible fluid flows," *Numer. Heat Transfer* **7**, 147–163 (1984).
- ⁴⁸O. Ubbink and R. Issa, "A method for capturing sharp fluid interfaces on arbitrary meshes," *J. Comput. Phys.* **153**, 26–50 (1999).
- ⁴⁹J. U. Brackbill, D. B. Kothe, and C. Zemach, "A continuum method for modeling surface tension," *J. Comput. Phys.* **100**, 335–354 (1992).
- ⁵⁰B. Lafaurie, C. Nardone, R. Scardovelli, S. Zaleski, and G. Zanetti, "Modelling merging and fragmentation in multiphase flows with SURFER," *J. Comput. Phys.* **113**, 134–147 (1994).
- ⁵¹J. Göhl, A. Mark, S. Sasic, and F. Edvelik, "An immersed boundary based dynamic contact angle framework for handling complex surfaces of mixed wettabilities," *Int. J. Multiphase Flow* **109**, 164–177 (2018).
- ⁵²M. M. Francois, S. J. Cummins, E. D. Dendy, D. B. Kothe, J. M. Sicilian, and M. W. Williams, "A balanced-force algorithm for continuous and sharp interfacial surface tension models within a volume tracking framework," *J. Comput. Phys.* **213**, 141–173 (2006).
- ⁵³P. Bartholomew, F. Denner, M. H. Abdol-Azis, A. Marquis, and B. G. van Wachem, "Unified formulation of the momentum-weighted interpolation for collocated variable arrangements," *J. Comput. Phys.* **375**, 177–208 (2018).
- ⁵⁴K. Konstantinidis, J. Göhl, A. Mark, and S. Sasic, "Coalescence-induced jumping of microdroplets on superhydrophobic surfaces—A numerical study," *Can. J. Chem. Eng.* **100**, 3517–3530 (2022).
- ⁵⁵S. F. Kistler, "Hydrodynamics of wetting," in *Wettability*, Vol. 6, edited by J. Berg (CRC Press, 1993), Chap. VI, pp. 311–430.
- ⁵⁶R. L. Hoffman, "A study of the advancing interface. II. Theoretical prediction of the dynamic contact angle in liquid-gas systems," *J. Colloid Interface Sci.* **94**, 470–486 (1983).
- ⁵⁷M. Jiang and B. Zhou, "Improvement and further investigation on Hoffman-function-based dynamic contact angle model," *Int. J. Hydrogen Energy* **44**, 16898–16908 (2019).

- ⁵⁸A. Marchand, J. H. Weijs, J. H. Snoeijer, and B. Andreotti, “Why is surface tension a force parallel to the interface?,” *Am. J. Phys.* **79**, 999–1008 (2011).
- ⁵⁹K. Washino, H. Tan, M. Hounslow, and A. Salman, “A new capillary force model implemented in micro-scale CFD–DEM coupling for wet granulation,” *Chem. Eng. Sci.* **93**, 197–205 (2013).
- ⁶⁰G. T. Nguyen, E. L. Chan, T. Tsuji, T. Tanaka, and K. Washino, “Interface control for resolved CFD–DEM with capillary interactions,” *Adv. Powder Technol.* **32**, 1410–1425 (2021).
- ⁶¹N. M. Newmark and F. Asce, “A method of computation for structural dynamics,” *J. Eng. Mech. Div.* **85**, 67–94 (1959).
- ⁶²E. Milacic, M. W. Baltussen, and J. A. Kuipers, “Direct numerical simulation study of droplet spreading on spherical particles,” *Powder Technol.* **354**, 11–18 (2019).
- ⁶³D. Legendre and M. Maglio, “Numerical simulation of spreading drops,” *Colloids Surf., A* **432**, 29–37 (2013).
- ⁶⁴J. C. Bird, S. Mandre, and H. A. Stone, “Short-time dynamics of partial wetting,” *Phys. Rev. Lett.* **100**, 234501 (2008).
- ⁶⁵L. Courbin, J. C. Bird, M. Reyssat, and H. A. Stone, “Dynamics of wetting: From inertial spreading to viscous imbibition,” *J. Phys.: Condens. Matter* **21**, 464127 (2009).
- ⁶⁶S. Mitra, M. J. Sathe, E. Doroodchi, R. Utikar, M. K. Shah, V. Pareek, J. B. Joshi, and G. M. Evans, “Droplet impact dynamics on a spherical particle,” *Chem. Eng. Sci.* **100**, 105–119 (2013).